Pergamon

Int. Comm. Heat Mass Transfer, Vol. 26, No. 2, pp. 165–176, 1999

0735-1933/99/$–see front matter

PII S0735-1933(99)00003-2

ENDWALL EFFECT ON THE MASS TRANSFER IN A SQUARE OPEN CAVITY

Ping-Hei Chen
Department of Mechanical Engineering
National Taiwan University
Taipei, Taiwan, R.O.C.

Jr-Ming Miao
Department of Mechanical Engineering
Chung Cheng Institute of Technology
Taoyuan, Taiwan, R.O.C.

(Communicated by J.P. Hartnett and W.J. Minkowycz)

ABSTRACT

In a lid-driven flow over a square open cavity with confined endwalls, a naphthalene sublimation technique was employed to measure the local mass transfer rates over the bottom surface of the cavity for the Reynolds numbers ranging from 2,000 to 4,000. The tested cavity has a span-to-width ratio (*SAR*) of 8 and a width-to-depth ratio (*AR*) of 1. The measured results are compared with predictions based on a deterministic vortex method with the assumption of two-dimensional cavity flow. The numerical results indicate an increase in mass transfer rate on the bottom surface of the cavity with an increase in the Reynolds number. The experimental results show the similar trend in the mass transfer rate with the presence of endwalls. In addition, a large variation in the spanwise direction of the measured local mass transfer rates implies the existence of Taylor – Görtler - like (*TGL*) vortices in the cavity. Furthermore, a correlation is derived between the measured overall averaged Sherwood number and the Reynolds number. © 1999 Elsevier Science Ltd

Introduction

Convective transport phenomena in shear-driven cavity flow has been observed in many engineering applications, such as the heat diffusion problem in the heat exchanger systems and the heat diffusion problem in the crystal growth, the cooling problem of integrated circuits, and the etching problem in the

fabrication of thin-film elements. Because of the simple geometry of the cavity and the easily controllable boundary conditions [1], the flow field structure and the heat (mass) transfer phenomena, in case of the shear-driven flow over a two-dimensional cavity, often can serve as a benchmark for assessment of developing numerical schemes.

A number of experimental and numerical studies have been conducted to investigate the flow field and heat transfer characteristics of lid-driven cavity flows in the last several decades. Flow visualizations and velocity measurements in lid-driven flow over a closed cavity with various *SAR* values were performed by Koseff and Street [2,3] and Prasad and Koseff [4]. The effect of the endwalls on the flow field development in the cavity was also assessed in their sequential studies. In addition to a downstream secondary eddy in the symmetric plane of cavity, some Taylor–Görtler-like (*TGL*) vortices were observed near the downstream lower corner in the vertical plane (normal to the flow direction), as indicated by the rheoscopic fluid streaks in their flow visualization results for the $SAR = 3$ case. Near the lower corner of the vertical endwalls, corner vortices were formed due to a spiral motion of the downstream secondary eddy moving from the symmetric plane to the endwalls. Numerical studies have also been conducted, Iwatsu et al. [5] employed a finite-difference scheme to predict the flow field driven by a sliding top wall in a cubic cavity. Their numerical results demonstrate the existence of *TGL* vortices [2]. Jordan and Ragab [6] employed a direct numerical method to simulate the three-dimensional shear-driven cavity flow. Rahman and Carey [7] conducted their numerical investigation on an open cavity with a moving top wall to study the mixed heat transfer problem in the cavity. With the buoyancy effect in the etching process, Shin and Economou [8] investigated the mixed convection mass transfer problem in a two-dimensional open cavity with various *AR* values.

However, all the prior studies that focused on the convective transport phenomena in a cavity are limited to the steady-state case or to the case in a two-dimensional cavity flow. The aim of present study is to investigate the effect of the endwalls on the mass/heat transfer distribution over the bottom surface of an open cavity with $SAR = 8$ and $AR = 1$ as a linear shear-driven flow passes over the top of cavity. Experimental measurements were conducted using the naphthalene sublimation technique. For comparison, a deterministic vortex method [9] was also employed to solve the two-dimensional and unsteady Navier-Stokes equations with same boundary conditions as the experimental runs in order to obtain the steady state mass transfer distributions on the bottom surface of cavity.

Numerical Simulation and Experimental Facility

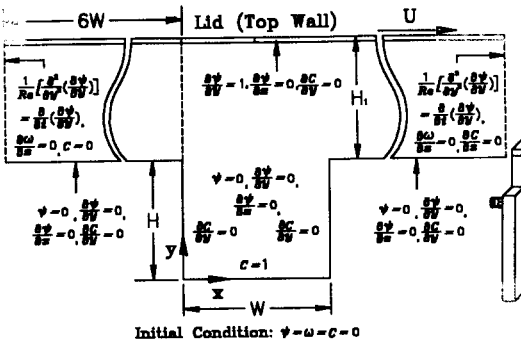

FIG. 1
A schematic view of the mass transfer problem in the two-dimensional and open cavity with $AR = 1$

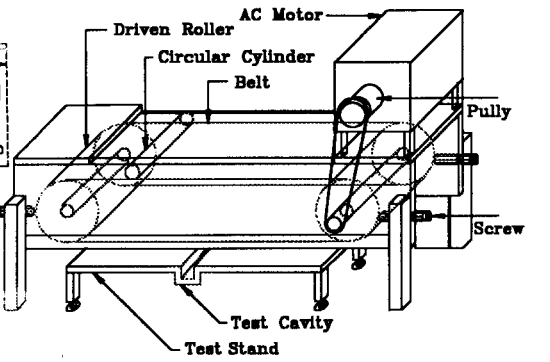

FIG. 2
A schematic view of the experimental test rig.

Figure 1 shows the schematic view of the configuration of the two-dimensional and open cavity for which the mass transfer problem was solved using a deterministic vortex method with second-order accuracy in both time and space. The initial condition and the boundary conditions are also shown in Fig. 1. The value of channel height, H_1, is chosen to be the same as the cavity height, H. The flow field in the cavity is assumed to be two-dimensional and laminar. In addition, the fluid is considered to be incompressible and Newtonian. Initially, a step speed of U was applied to the lid and the cavity floor was then given a step change in concentration. At locations far away from the cavity body, the channel flow between the lid and the upstream and downstream flat walls can be treated as an instantaneously started plane Couette flow. In all mass transfer runs, only the cavity floor is coated with a layer of solid naphthalene and the other cavity walls are naked metal. Therefore, the corresponding heat transfer boundary conditions for such a cavity system can be regarded as isothermal on the cavity floor and adiabatic on the other cavity walls.

To describe the mass transfer and flow field problems in a lid-driven flow system, the non-dimensional continuity equation and momentum equation in forms of stream function and vorticity function are expressed as follows:

$$\nabla^2 \psi = -\omega \tag{1}$$

$$\frac{\partial \omega}{\partial t} + (\boldsymbol{u} \bullet \nabla)\omega = \frac{1}{Re}\nabla^2 \omega \tag{2}$$

The non-dimensional mass concentration equation is given by

$$\frac{\partial C}{\partial t} + (\boldsymbol{u} \bullet \nabla)C = \frac{1}{Sc \bullet Re}\nabla^2 C \tag{3}$$

The operation principle of the deterministic vortex method is to split the momentum equation in vorticity form (Eq. (2)) into a convection term and a diffusion term. A detailed description of the entire procedure for solving the momentum equation in vorticity form (Eq. (1)) can be found in [9]. The present study uses the same procedure to solve the mass concentration equation (Eq. (3)), as well. An 111×131 non-uniform grid mesh in the cavity body was used throughout the whole study based on the grid-independence test among grid meshes of 101×121, 111×131, and 121×141. Also, a time-step, Δt, of 0.02 was selected after a time-step test for Δt = 0.01, 0.02, and 0.04. The inlet and outlet of the channel flow were placed at locations six times the cavity width (W) away from the cavity opening, shown in Fig. 1, so that the flow development in the cavity body would not be retarded. In comparisons of the predicted values with experimental data obtained from the naphthalene sublimation technique, the Schmidt number, Sc, was taken as 2.2. The criteria under which the physical system reached steady state for stream function, mass concentration, vorticity, and Sherwood Number were given as 10^{-4}, 10^{-4}, 2×10^{-3}, and 3×10^{-5} respectively.

To study the detailed mass transfer distributions on the cavity floor, a naphthalene sublimation technique was employed [10]. A schematic view of the experimental test rig for the lid-driven flow system is shown in Fig. 2. The test cavity was assembled with two vertical upstream and downstream walls and one cavity floor, all made of an aluminum alloy. The test cavity has a height of 1.5 cm, a width of 1.5 cm, and a span of 12 cm., ie. H/W = 1 and SAR = 8. The bottom surface of the test cavity was roughened by drilling grooves in order to hold the coated naphthalene surface. After a careful casting procedure, a layer of solid naphthalene with a thickness of 1.5 mm was cast onto the surface of the cavity floor. In addition, a calibrated T-type thermocouple was embedded underneath the solid naphthalene. The temperature readings from this thermocouple were used to determine the diffusion coefficient of naphthalene into air based on the correlation suggested in [10]. The temperature variation for a typical mass transfer run was approximately ± 0.3 °C.

After the test cavity was tightly fit onto the central portion of the test stand, two plexiglas plates were attached onto both sides of the test cavity to serve as the endwalls. The speed of the plastic belt (serving as the "lid") was controlled by the AC motor coupled with a variable speed controller. The smooth motion of the plastic belt is assured by four small circular cylinders with adjustable screws located at the four corners of the test rig. In addition, a circular cylinder is placed onto the belt surface to reduce the vibration of belt, as shown in Fig. 2. By proper adjustment, the vibration of the plastic belt in the vertical direction can be controlled within to ± 0.5 mm during operation. Underneath each leg of the test stand, there is a screw that can be adjusted separately to assure the required channel height between the belt and the level of the flat

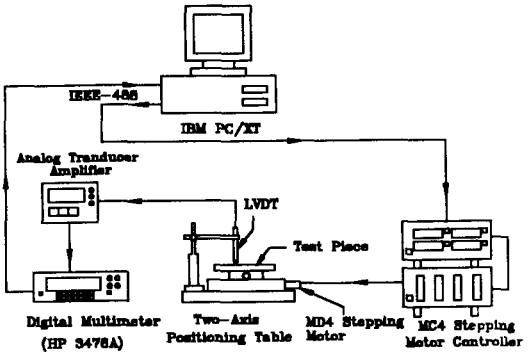

FIG. 3
A schematic view of the two-axis automated measuring system.

surface. The rotating frequency of the driving roller was measured by counting the number of impulses of light received from reflective tape on the belt by an optical sensor with a digital display. The uncertainty in measured rotating frequency is ± 1 rpm. Once the rotating frequency, f, of the belt is measured, the Reynolds number can be calculated by

$$Re = \frac{UW}{\nu} = \frac{1}{60} \times \frac{fLW}{\nu} \tag{4}$$

The local mass transfer rate was determined from the sublimation depth of the coated naphthalene on cavity floor after it was exposed in the lid-driven flow over a period of time. To determine the sublimation depth, the naphthalene surface profiles of the test piece before and after each test run were measured. A PC-controlled two-axis automated measuring system was used to measure the surface profiles. Figure 3 shows a schematic view of the two-axis automated measuring system which consists of a depth gauge (LVDT), a two-axis positioning table, a motor controller, two stepping motors, a linear signal conditioner, a digital multimeter, and a PC-XT computer. The LVDT(linear variation differential transformer), made by PRETEC Co. (Model 1920), has a measurement range of 1.0 mm with a 0.1 μm resolution, which is more than sufficient for the typical average sublimation depth in a mass transfer run of around 78 μm. The local mass transfer coefficient on the test surface is defined as

$$h_m = \frac{L_{sb}\rho_s}{\rho_{v,w}\Delta t} \tag{5}$$

where L_{sb} is the sublimation depth, ρ_s is the density of solid naphthalene and Δt is the duration of test time. The $\rho_{v,w}$ value can be resolved from the ideal gas law once the vapor pressure and the temperature of naphthalene are known. The vapor pressure was determined using an empirical correlation given in [11]. The total sublimation depth on each measured location was determined from two surface profile

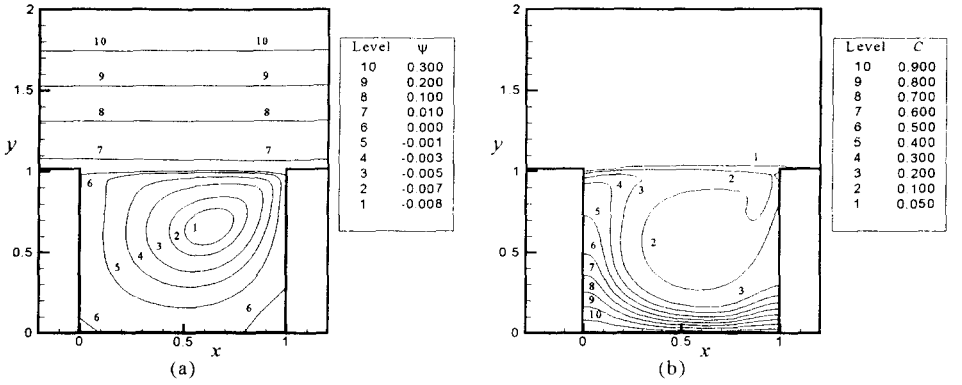

FIG. 4
The steady state two-dimensional numerical results for the case of Re = 3,000;
(a) flow field, (b) concentration field

measurements one before and one after the test piece was exposed to the air-stream. However, the total sublimation depth cannot be simply substituted into Eq. (5) because some extraneous sublimation losses may occur during the surface profile measurements on the two-axis positioning table or during the installation of the test piece into the test rig. A detailed description of the procedure to obtain these losses could be found in [10]. In this study, the major uncertainty in the mass transfer coefficient is attributed to natural convection and temperature variation during the mass transfer run. The mass transfer coefficient can also be non-dimensionalized as the Sherwood number,

$$Sh = \frac{h_m W}{D_f} \tag{6}$$

Mass transfer measurements were conducted at three different plastic belt speeds, corresponding to Reynolds numbers of 2,000, 3,000, and 4,000. In each mass transfer run, the mass transfer results are measured at 39 streamwise locations on the test piece, extending from x = 0.025 to x = 0.975. At each streamwise location, there are 27 measuring points along the spanwise direction, spanning from z = -3.92 to z = 3.92. Based on the 95% confidence level and the equation proposed by Kline and McClintock [12] for single-sample experiments, the uncertainties in measured Sh and Re values are ± 8.5% and ± 5%, respectively. In addition, the repeatability of the mass transfer measurement was checked by conducting several experiments for each test case.

Results and Discussion

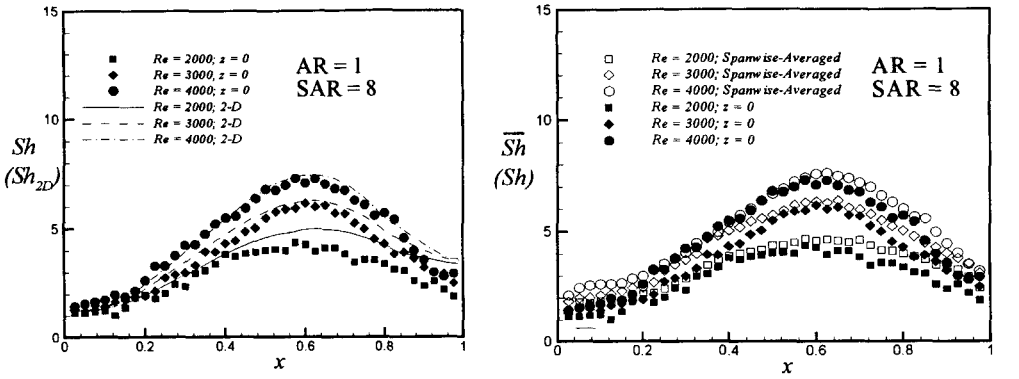

(a) (b)

FIG. 5
A comparison between the measured results on the symmetric plane of the cavity along the streamwise direction; (a) numerical results, (b) experimental spanwise-averaged results.

Predicted Results for a Two-Dimensional Lid-Driven Flow Over an Open Cavity

Figures 4(a) and 4(b) respectively show the numerical predicted flow field and concentration field in the cavity at Re = 3,000 as the physical system reaches the steady state. As shown in Fig. 4(a), near-parallel streamlines in the channel demonstrate that the channel flow is only slightly affected by the presence of the cavity body. The flow field elements in the present open cavity are similar to that of a closed cavity [2]. It can be clearly observed that one primary vortex occupies the largest portion of the cavity body, and there are also two secondary eddies, located at the upstream and downstream lower corners. The formations of the upstream secondary eddy (*USE*) and the downstream secondary eddy (*DSE*) result from the separation and reattachment of the boundary-layer flow that is driven by the motion of the primary vortex. When the boundary-layer flow on the downstream vertical cavity wall moves downwards to the downstream lower corner, the boundary-layer flow separates from the wall surface due to the presence of strong adverse pressure gradient near the corner. Following the separation, the boundary-layer flow quickly reattaches to the bottom surface of cavity. The situation for the formation of upstream secondary eddy near the upstream lower corner is similar to that for the formation of downstream secondary eddy. Figure 4(b) shows that the mass transfer rates over the cavity surfaces are dominated by the motion of primary vortex. On both upstream and downstream vertical walls of the cavity, the iso-concentration lines are normal to the cavity surfaces due to the impermeable boundary conditions. In the lower half of the cavity body, dense iso-concentration lines can be observed near the center location ($x \approx$ 0.65). These dense iso-concentration lines are caused by the acceleration of boundary-layer flow and thus signify a high mass transfer rate. On the other hand, a slow velocity of the upstream secondary eddy results

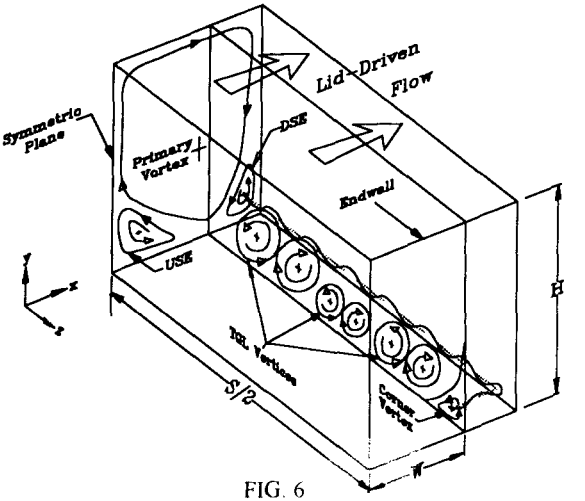

FIG. 6
A sketched flow field in the three-dimensional cavity.

in a low mass transfer rate at the upstream lower corner ($x = 0$). Since the major characteristics of the flow field (i.e. one primary vortex and two secondary eddies) in the cavity are little affected by the variation in the Reynolds number, the plots of flow and concentration fields at Reynolds numbers other than 3,000 are not presented in this paper.

Experimental Results in an Open Cavity With $SAR = 8$ and $AR = 1$

Figure 5(a) shows the comparison between the numerical and experimental results over the cavity floor at various Reynolds numbers. In Fig. 5(b), the local Sherwood number along the streamwise direction on the symmetric plane of cavity (i.e. $z = 0$) is compared against the spanwise-averaged Sherwood number at various Reynolds numbers. In both figures, the experimental results with solid symbols are the local Sherwood number distributions on the symmetric plane of the cavity. A good agreement in the trend of mass transfer distribution with an increase of Reynolds number can be observed between the predicted results from the two-dimensional simulation and the measured mass transfer results on the symmetric plane of cavity, as indicated from Fig. 5(a). Due to the presence of endwalls, the measured mass transfer results on the symmetric plane of cavity are slightly lower than the predicted values. More specifically, for the present test cavity with a large span-to-width ratio (SAR) of 8, the three-dimensional flow characteristics (e.g. corner vortices and TGL vortices), observed by Koseff and Street [2,3], still exist and result in the lower measured mass transfer rates on the symmetric plane of cavity than the two-dimensional predictions. The evidence of three-dimensional flow characteristics in the cavity will be illustrated from the spanwise

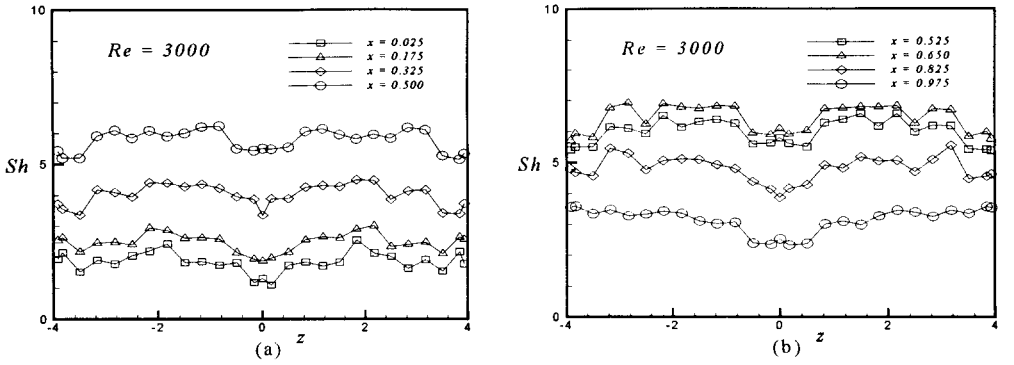

FIG. 7
The spanwise distributions of measured local Sherwood number on the bottom floor of cavity at different streamwise positions for the case of Re = 3,000; (a) x = 0.025-0.5, (b) x = 0.525-0.975

distributions of the local Sherwood number in a later section. On the bottom surface, the highest mass transfer rate is expected to occur at the location where the separation of the primary vortex from the downstream vertical cavity wall is reattached. The location with the maximum Sh value does not vary with an increase in the Reynolds number. In other words, the reattachment point of the primary vortex on the bottom surface of the cavity was negligibly affected by the increase of the Reynolds number.

Figure 5(b) shows that the spanwise-averaged mass transfer rates are higher than the local mass transfer rate on the symmetric plane of cavity at the same Reynolds number. Such a difference between local and spanwise-averaged mass transfer rates is caused not only by the corner vortices near the endwalls but also by the *TGL* vortices in the cavity. The correlation for the predicted averaged Sherwood number ($\overline{Sh_{2D}}$) and the measured overall averaged Sherwood number ($\overline{\overline{Sh}}$) versus the Reynolds number (Re) for a lid-driven flow over an open cavity with SAR = 8, AR = 1, H_1/H = 1, and Sc = 2.2 can be evaluated and given by

$$\overline{Sh_{2D}} = 0.0419 Re^{0.57} \tag{7}$$

$$\overline{\overline{Sh}} = 0.0446 Re^{0.57} \tag{8}$$

Both equations are valid in a range of 2,000 ≤ Re ≤ 4,000. The deviation in predicted values evaluated from Eqs. (7) and (8) is less than 10%.

Figure 6 shows the flow field in a cavity confined with endwalls. The flow field is sketched based on both the flow visualization results with SAR ranging from 1 to 3 [3,6] and the present two-dimensional

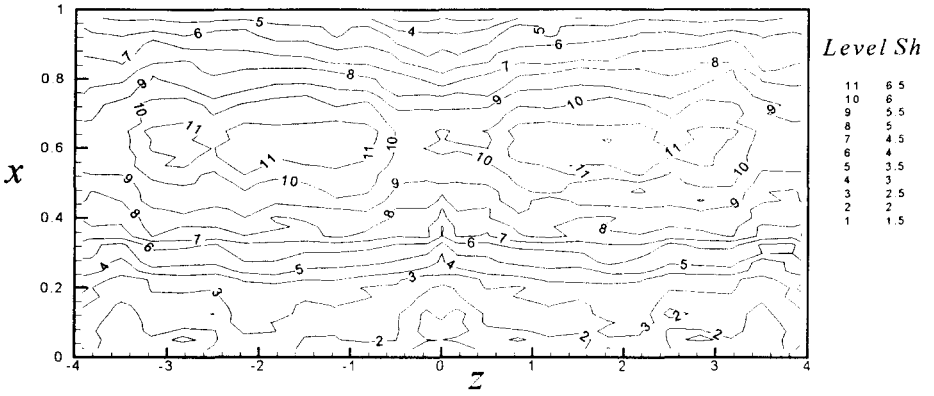

FIG. 8
A contour plot of measured local Sherwood number distributions on the bottom floor of cavity for case of Re = 3,000.

numerical results. It can be seen that the formation of the corner vortex near the endwall results from the spiral motion of the downstream secondary eddy. For a cavity with a smaller SAR value than that in the present study, both flow visualization results [3] and numerical predictions [6] on the vertical plane at x = 0.77 demonstrated the appearance of TGL vortices. All of these vortices do significantly affect the mass transfer rate over the cavity floor. Figures 7(a) and 7(b) show the measured local Sherwood number distributions on the bottom surface of cavity at different streamwise locations for the case of Re = 3,000. The visible wavy distribution of local Sherwood number along the spanwise direction can be observed over the whole bottom surface of the cavity. Repeatability runs were executed and demonstrated that the wavy behavior in the local mass transfer rates consistently appeared. This wavy behavior provides the evidence that the flow field in the cavity is actually not expected to be two-dimensional. Near the endwalls, the rise in the mass transfer rate is due to the effect of corner vortices. Along the spanwise direction, the local minimum in Sh could be attributed to the up-wash of two counter-rotating vortices. Similarly, a peak in local mass transfer rate could result from the down-wash of two counter-rotating vortices. Since the trend in the local Sherwood number distributions for cases of other Reynolds numbers are similar to those presented in Figs. 7(a) and 7(b) for the case of Re = 3,000, the local mass transfer rates at other Reynolds numbers are not presented here. For the case of Re = 3,000, a contour plot of the local Sherwood number distributions on the bottom surface of cavity is shown in Fig. 8. These contour lines shown in Fig. 8 are interpolated from the measured local Sherwood number distributions. Only the mass transfer rate on half of the bottom surface of the cavity is shown in Fig. 8 because of the symmetry of measured results about the plane of z = 0. The closed contour lines in regions of $0.5 < x < 0.7$ indicate the existence of TGL vortices.

Conclusions

Mass transfer measurements were conducted by using the naphthalene sublimation technique to investigate the effect of the endwalls on the mass transfer distributions over the bottom floor of an open lid-driven flow cavity with SAR = 8, AR = 1, and H_1/H = 1. The test Reynolds number ranges from 2,000 to 4,000. In addition, a deterministic vortex method was used to solve the flow field and mass transfer problem with the same boundary conditions as the experimental runs. Comparisons between the experimental results and the numerical results were made. Some conclusions can be drawn from the present investigation.

(1) Over the cavity bottom surface, the difference in the two-dimensional predicted results and the measured local mass transfer results on the symmetric plane of cavity at SAR = 8 is noticeable due to the three-dimensional flow field in the cavity. Particularly, the difference is greatest in regions near the upstream and downstream vertical wall corners. The closed contour lines at $0.5 < x < 0.7$ indicate the presence of Taylor – Görtler - like vortices.

(2) The streamwise location with the maximum value in the spanwise-averaged mass transfer rate is varied little with the Reynolds number.

(3) Both the numerical predicted results and the measured results indicate an increase in mass transfer rate on the bottom surface of the cavity with an increase in the Reynolds number.

(4) A correlation between the measured overall averaged mass transfer rate on the cavity floor and the Reynolds number was evaluated to be $\overline{\overline{Sh}} = 0.0446Re^{0.57}$, which is valid in regions of Re = 2,000 to 4,000 for the lid-driven open cavity with SAR = 8, AR = 1, H_1/H = 1, and Sc = 2.2.

Acknowledgments

The authors like to express their appreciation for the financial support by the NSC under the Grant No. NSC 81-0401-E002-236.

Nomenclature

AR height to width ratio

D_f diffusion coefficient of naphthalene into air [m^2s^{-1}]

SAR span to width ratio

Sh local Sherwood number

Sh_{2D} predicted local Sherwood number

$\overline{Sh}$ spanwise-averaged Sherwood number

$\overline{Sh_{2D}}$ predicted averaged Sherwood number

$\overline{\overline{Sh}}$ overall averaged Sherwood number

$\boldsymbol{u}$ dimensionless velocity vector

x horizontal coordinate; $x = 0$ on the upstream cavity vertical wall

z coordinate in the spanwise direction, $z = 0$ on the symmetric plane

Greek Symbol

ψ dimensionless stream function

ω dimensionless vorticity

References

1. J.W. Goodrich and W.Y. Soh, *J. Comp. Phy.* **84**, 207 (1989).

2. J.R. Koseff and R.L. Street,. ASME *J. of Fluids Eng.* **106**, 521(1984).

3. J.R. Koseff and R.L. Street, ASME *J. of Fluids Eng.* **106**, 385 (1984).

4. A.K. Prasad and J.R. Koseff, *Phys. Fluids Part A.* **1**, 208 (1989).

5. R. Iwatsu, J.M. Hyunm, and K. Kuwahara, *Fluid Dynamics Res.* **6**, 91 (1990).

6. S.A. Jordan and S.A. Ragab, ASME *J. of Fluids Eng.* **116**, 439 (1994).

7. M. Rahman and G.F. Carey, *Numerical Heat Transfer* **25**, 85 (1994).

8. C.B. Shin, and D.J. Economou, *Int. J. Heat Mass Transfer* **33**, 2191 (1990).

9. C.C. Chang and R.L. Chern, *J. of Fluid Mech.* **233**, 243 (1991).

10. R.J. Goldstein and H.H. Cho, *Experimental Thermal and Fluid Science* **10**, 416 (1995).

11. D. Ambrose, I.J. Lawrenson, and C.H.S. Sprake, *J. Chem. Thermodynamics* **7**, 1173 (1975).

12. S.J. Kline and F.A. McClintock, *J. Mech. Eng.* **75**, 3 (1953).

Received July 25, 1998